Dynamic compound wavelet matrix method for multiphysics and multiscale problems

Krishna Muralidharan,[1] Sudib K. Mishra,[2] G. Frantziskonis,[2,1] P. A. Deymier,[1] Phani Nukala,[3] Srdjan Simunovic,[3] and Sreekanth Pannala[3]

[1]*Department of Materials Science and Engineering, University of Arizona, Tucson, Arizona 85721, USA*

[2]*Department of Civil Engineering and Engineering Mechanics, University of Arizona, Tucson, Arizona 85721, USA*

[3]*Computer Science and Mathematics Division, Oak Ridge National Laboratory, Oak Ridge, Tennessee 37831, USA*

(Received 29 August 2007; revised manuscript received 6 December 2007; published 29 February 2008)

The paper presents the dynamic compound wavelet method (dCWM) for modeling the time evolution of multiscale and/or multiphysics systems via an "active" coupling of different simulation methods applied at their characteristic spatial and temporal scales. Key to this "predictive" approach is the dynamic updating of information from the different methods in order to adaptively and accurately capture the temporal behavior of the modeled system with higher efficiency than the (nondynamic) "corrective" compound wavelet matrix method (CWM), upon which the proposed method is based. The system is simulated by a sequence of temporal increments where the CWM solution on each increment is used as the initial conditions for the next. The numerous advantages of the dCWM method such as increased accuracy and computational efficiency in addition to a less-constrained and a significantly better exploration of phase space are demonstrated through an application to a multiscale and multiphysics reaction-diffusion process in a one-dimensional system modeled using stochastic and deterministic methods addressing microscopic and macroscopic scales, respectively.

DOI: 10.1103/PhysRevE.77.026714 PACS number(s): 02.70.−c, 89.20.−a

I. INTRODUCTION

The scientific and engineering problems that span and couple multiple temporal and spatial scales are usually analyzed within the framework of multiscale methods. The efficacy of these techniques relies on their ability to combine appropriate information while obeying conservation laws when different scale-specific submethods are coupled. Many numerical frameworks have been proposed explicitly towards this, such as the heterogeneous multiscale method (HMM) [1], quasicontinuum method [2], equation-free coarse-grained multiscale method [3], coarse-grained molecular dynamics [4], molecular-atomistic *ab initio* dynamics (MAAD) [5], wavelet-based compound wavelet matrix (CWM) [6–9], and parallel-in-time method [10]. Of particular interest is the CWM method, which takes advantage of the inherent capabilities of wavelets bases to represent physical phenomena in a multiscale fashion.

The ability of wavelets to separate scale information effectively through the construction of local orthogonal basis functions makes them invaluable in the examination of local, global, and scalewise properties of any data set (or signal) that requires multiresolution analysis. As examples, such data could represent fractals, multifractals, turbulence patterns, or earthquakes [11–13]. In such applications, typically, wavelets operate on a signal obtained from a method restricted to a single discretization in time and/or space. CWM differs from such multiresolution techniques in that it bridges solutions obtained from multiple methods operating on different discretizations in time and space to yield a composite multiscale representation, while using wavelets as the basis. Utilizing wavelets as a multiscale tool rather than a pure multiresolution tool makes the CWM approach a *unique* as well as a *powerful* technique for coupling disparate simulation methods that address the same process, albeit at different levels of accuracy, or, equivalently different levels of theory. CWM also differs from up-scaling techniques [14,15] used in adaptive bridging of scales, given that in the CWM framework, physical phenomena are examined using two or more different methods at their respective scales not necessarily based on the same variables or in the same mathematical form.

In its original formulation, CWM was conceived as a multiscale tool for combining short-time (and/or small spatial domain) fluctuations that could only be obtained from computationally expensive fine-scale methods, with the large-scale long-time (and/or large spatial domain) mean behavior of coarse-scale method(s), while assuming stationarity for the fluctuations in the overall trajectories. It has been applied to various multiscale phenomena such as grain-growth and microstructure evolution [6], heterogeneous porosity and inclusions [7], dispersion problems [8], and diffusion from a reactive boundary [9]; in these studies, the fine-scale and coarse-scale information were combined via a compound wavelet matrix to yield the coupled multiscale behavior of the system over the entire extent of space and time. In other words, CWM was used as a *corrective* tool, involving the transfer of fine-scale fluctuations of the accurate method on to the coarse-method trajectory. In this paper, the CWM is further generalized to serve as an accurate *predictive* tool, by extending it to take into account the interaction of the fine- and coarse-scale methods as the simulated system evolves in phase space.

The proposed dynamic CWM (dCWM) method extends the CWM approach by incorporating active coupling of different monoscale simulation methods, resulting in a dynamic evolution of the system under study. In other words, the system is simulated by a sequence of temporal increments where the CWM solution on each increment is used as the initial conditions for the next. Another equally important feature of this work is the improvements made to the compounding methodology, making it capable of projecting the shorter-fine trajectory in time, based on the relative magni-

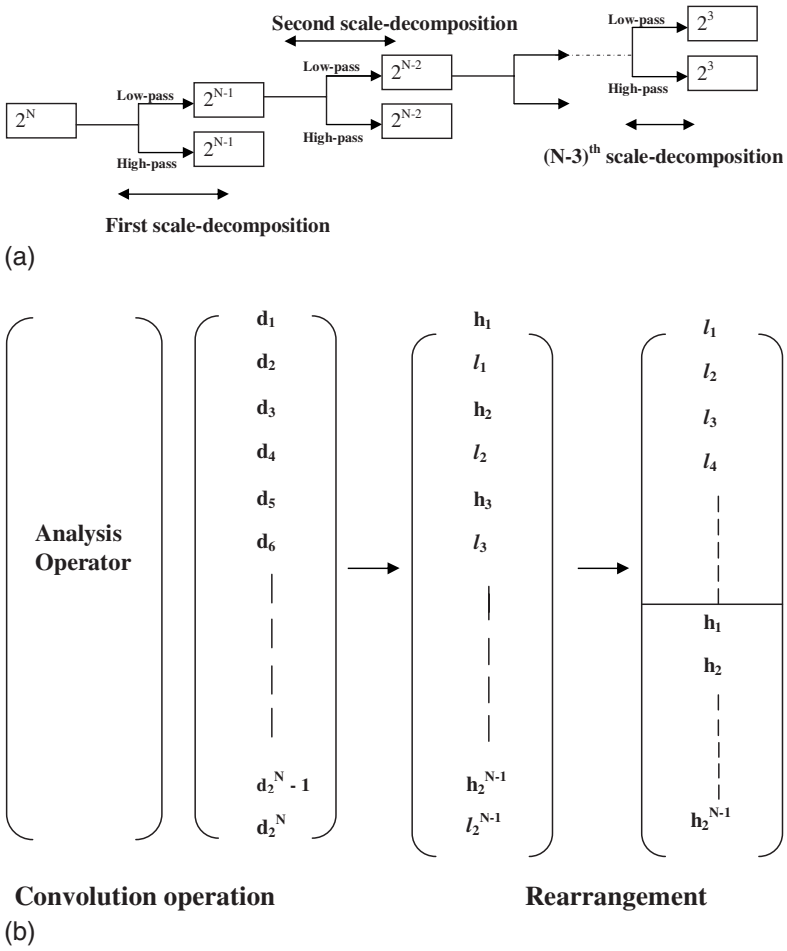

FIG. 1. (a) Stage by stage wavelet decomposition of a 2^N vector. At each stage, the data vector is convolved with two kinds of wavelet filters (low-pass and high-pass) resulting in two sets of wavelet-transformed data. (b) Illustration of the first stage of wavelet decomposition. The initial convolution operation is followed by rearrangement. Here h and l represent the high-pass and low-pass components, respectively.

tudes of the coarse-method and fine-method wavelet coefficients as explained in the following sections. The consequent advantages of using the dCWM method are illustrated via a "simple" one-dimensional (1D) model of a two-species reaction-diffusion process that is represented by two distinctive methods differing in their ability to describe the physics of the reaction-diffusion process.

II. MODELS AND METHODS

A. Wavelet bases for multiscale problems

A discrete function can be hierarchically transformed into wavelet space by using discrete wavelet transforms (DWT) [16–20] via a series of "scale decompositions" with each stage of decomposition representing a level of description of the function specific to that scale. The transforms involving a set of wavelet filters in the form of linear convolution operators are applied hierarchically first to the full data vector (assuming the discrete function to be a 1D data vector of length 2^N), then to a smoother vector of length 2^{N-1}, then to a vector of length 2^{N-2}, and so on and so forth [as shown in Fig. 1(a)] until only a trivial number of smooth components (scaling or mother-function coefficients) remain; the number of scaling coefficients depend on the number of wavelet filters chosen. At any scale, the "h_i" components of the transformed vector [Fig. 1(b)], which are essentially decorrelated, represent the wavelet coefficients corresponding to that scale, and characterize the scale-specific fluctuations inherent to the original function. The inverse transform is the exact reverse of the above process, with the wavelet operator (analysis operator) replaced by its inverse (synthesis operator). Different boundary conditions (e.g., periodic, fixed, zero, or on the interval), are implemented by modifications of the appropriate operator terms [20].

Every scale-decomposition stage results in two sets of components: The smooth (or coarse) and the fine components, each representing a localized "moving" average of the function (in wavelet space) with the fine components being regarded as the "true" wavelet coefficients corresponding to the given scale. For convenience, at each stage, the data are rearranged as shown in Fig. 1(b). Since the hierarchical decomposition at each stage acts only on the smoother components of the previous stage, only very "coarse" information is available at the final stages of the wavelet transform procedure.

The given function (or signal) can be examined at any given range of scales simply by retaining the wavelet transform (WT) coefficients corresponding to the chosen scales and setting all other coefficients equal to zero and then sequentially reconstructing via the inverse transform to obtain a modified signal; this method is sometimes referred to as the padding technique. Extending these concepts, coupling of two different signals in wavelet space can be done by first

identifying their overlapping scales (spatial and temporal) and then substituting corresponding wavelet coefficients from each signal into a compound wavelet matrix (CWM) that can be inverted to provide a hybrid signal that has the desired characteristics of both signals over the union of scales of the two signals. The identification of the overlap is critical to the CWM method and the extent of overlap decides the relative accuracy of the hybrid signal as explained below.

B. Compounding methodology for coupling scales: Forming the CWM

Earlier implementations of CWM assumed no deviations in the overall trajectories as predicted by the different scale-specific methods modeling the given phenomenon. In this paper, the methodology presented is further generalized by taking into account any possible deviations between the different trajectories, thereby enhancing the ability to predict the true evolution of the system in phase space.

Without the loss of generality, the methodology will be described based on two temporally varying 1D signals, one representing the high-resolution, short-time trajectory—the fine signal, while the other corresponds to a coarse-resolution approximation obtained over a much longer time interval—the coarse signal. Let R denote the ratio of the size of the coarse (Δt_c) over the fine (Δt_f) time steps, and N_c and N_f represent the number of coarse and fine data points, respectively. The following steps result in a compound signal that contains essential information from both signals.

(1) *Coarse signal interpolation*. Depending on R, the coarse signal is interpolated in order to obtain a new signal with a larger set of data points (I_c), with the time interval between successive data points equaling Δt_f. Note that I_c equals the product of R and N_c.

(2) *Wavelet decomposition*. The wavelet transforms of the coarse and fine signals are performed until a trivial number of mother-wavelet or scaling coefficients (S_N) are left. If $S_N=8$ (2^3), then p_c-3, and p_f-3 scale decompositions are carried out on the coarse and fine signal, yielding I_c-8 and N_f-8 WT coefficients, respectively, where p_f and p_c are defined in Eq. (1):

$$I_c = 2^{p_c},$$

$$N_f = 2^{p_f}. \tag{1}$$

(3) *Selection and identification of overlapping scales*. Overlapping scales refer to common or equivalent scales between the two signals; given that 2^{pc} coarse data points and 2^{p_f} fine data points are sampled at the same rate (i.e., size of respective time steps are equal), the first p_f-3 scale decompositions for each signal are equivalent and yield $2^{(p_c-n)}$ and $2^{(p_f-n)}$ coefficients, respectively, at the nth scale decomposition (see Fig. 2).

(4) *Prolongation*. At all overlapping scales, the fine WT coefficients are replicated to ensure consistency in the number of coarse and fine WT coefficients. The number of replications M_p at a specific scale is given by $M_p=I_c/N_f$ and represents periodic repetitions of the fine fluctuations at every scale with the inherent assumption that the fluctuations are quasistationary over the period of coupling. The primary role of this step is to set the stage for replacement of a majority of the coarse coefficients by the repeated fine coefficients to enable the transferability of all fine information at every overlapping scale.

Fine			Coarse	
WT coefficient	**Timescales**		**WT Coefficient**	**Timescales**
			2^3	**8**
		coarse	2^3	$2^{(p_c-3)}t_f$
			.	
			.	
			.	
			.	
			.	
			.	
2^3	**8**		.	
2^3	$2^{(p_f-3)}t_f$		.	
.			.	
.			.	
.			.	
.			.	
.			.	
.			.	
			.	
			.	
			.	
			.	
			$2^{(p_c-4)}$	2^4t_f
$2^{(p_f-3)}$	2^3t_f		$2^{(p_c-3)}$	2^3t_f
$2^{(p_f-2)}$	2^2t_f		$2^{(p_c-2)}$	2^2t_f
$2^{(p_f-1)}$	2^1t_f		$2^{(p_c-1)}$	2^1t_f
Total $N_f=2^{p_f}$	2^0t_f		**Total** $I_c=2^{p_c}$	2^0t_f

FIG. 2. Tabulation of the number of overlapping scales and "coarse-only" scales for fine and coarse functions consisting of N_f and I_c data points.

(5) *Multiscaling via mixing and scaling of coefficients*. This stage enables an "intelligent" extension of the fine signal via appropriate selection of relevant wavelet coefficients at all scales from both signals to form a compound wavelet matrix (or vector in this case): In order to facilitate explaining the merging of coefficients, we will use for the coarse signal a smooth logarithmic function consisting of 1024 points (Fig. 3), while the shorter fine signal is comprised of the first 256 data points of the coarse signal with added white noise (via random numbers). Figure 4 presents (i) the WT of the coarse signal, (ii) WT of the first 256 points of same coarse signal (short-coarse), and (iii) WT of the fine signal; the above transforms use the symmetry-preserving bior-

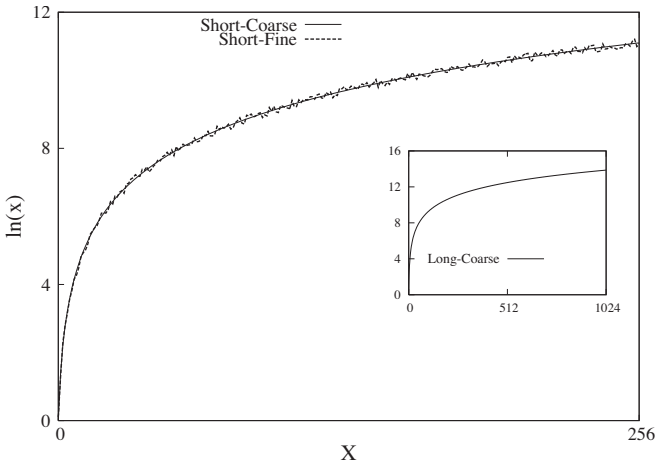

FIG. 3. Coarse and fine logarithmic signals used for explaining the dCWM process. The inset figure represents the entire coarse signal.

thogonal CDF(4,6) wavelet filters with on-the-interval boundary conditions [20]. Specifically, in Fig. 4, the values of the various coefficients at all scales of decomposition are given (except the first scale).

The following are clearly evident from Fig. 4: (i) The initial few and the final few coefficients of all the three signals at every scale are significantly different in magnitude from the rest of the coefficients, (ii) excluding the final few coefficients, the $2^{(p_f-n)}$ coefficients of the shorter coarse signal and the first $2^{(p_f-n)}$ coefficients of the larger coarse signal (where n refers to the nth scale decomposition, and $2^{p_f}=256$) at equivalent scales are identical, and (iii) the fine coefficients are slightly larger in magnitude than the corresponding short-coarse coefficients at every scale.

The difference in magnitude between the initial (or final) few coefficients and the rest is due to the imposition of boundary conditions, which contribute significantly to the net magnitude of the boundary (i.e., the initial and final few) coefficients [20]. The fact that there is a one-to-one match between the short-coarse and the corresponding long-coarse coefficients (barring the final few coefficients) at every equivalent scale is a consequence of the moving average representation characteristic of wavelets. The deviations between corresponding short-coarse and fine coefficients are a measure of the fluctuations (in this case, the white noise) inherent to the fine signal as also any possible deviations in the overall trajectories of the coarse and fine trajectories (in this case, the overall trajectory is the same).

While boundary conditions do change the initial and final coefficients at each scale significantly, it has to be noted that when both short and long coarse signals are wavelet transformed, the initial coefficients are the same, while it is only the final coefficients that differ; this is due to the fact that the same domain is sampled via the convolution operation to yield the initial coefficients while the longer-time data is not available to the shorter signal resulting in differences in the magnitudes of the final boundary coefficients.

The repetition of fine coefficients at overlapping scales, replicates the essentially uncorrelated fluctuations associated with the fine signal over the entire domain of the long, coarse signal. This repetition has to be done with care to (i) prevent any unphysical behavior that could arise due to the periodic appearance of the boundary coefficients at each scale, while (ii) ensuring appropriate boundary conditions are still imposed. One could identify these boundary coefficients either from the knowledge of the extent (length) of the boundary elements in the analysis and synthesis matrix or by adopting an empirical procedure: At each scale, the deviation in magnitude between corresponding short-coarse and short-fine coefficients averaged over all coefficients (except for the first and last) is calculated. The number of boundary coefficients is identified as the number of successive coefficients greater in magnitude than the average deviation calculated for that given scale. Typically, for the interval boundary conditions used herein, the first three and the last three coefficients represent the boundary coefficients.

After replication, any fine coefficient that is greater in magnitude than the average deviation is replaced by the corresponding long-coarse coefficient, except at certain locations, as explained below.

For clarity, consider the second equivalent scale decomposition of the long-coarse (i.e., coarse) and short-coarse signal [Figs. 4(g)]. Only the first 61 (=64−3) coefficients are identical, while the 62nd, 63rd, and 64th coefficients are obviously different, though, in fact, the ratios of the respective boundary coefficients (i.e., ratio of 254–256 of long-coarse to the 62–64 of short-coarse) are very similar (analogous trends are true for all other equivalent scales too). In order to transfer the entire spectrum of fine information available at this scale, and to ensure that only the true fine signal fluctuations and trends are periodically replicated, an initial repetition of all (in this case $M_p=4$) fine coefficients; next the 62–67, 126–131, and 190–195 of the repeated fine coefficients (corresponding to the boundary coefficients) are replaced by the equivalent coarse coefficients that are scaled by a multiplicative factor; this factor equals the ratio of the sum of absolute magnitudes of the short-fine coefficients to the sum of absolute magnitudes of the short-coarse coefficients, with the boundary coefficients being excluded in the respective sums.

Keeping in mind that the ratio of the end boundary conditions of the respective signals at each scale are comparable, the 254th, 255th and 256th fine coefficients are scaled by a factor $Es(1,2,3)$, where $Es(1,2,3)$ are the ratios of 254th long-coarse to 62nd short-coarse, 255th to 63rd and 256th long-coarse to 64th short-coarse coefficients, respectively. In a similar fashion, the above algorithm is repeated for all other overlapping scales too.

After appropriate repetitions and replacements at every overlapping scale, 32 remaining coarse coefficients are available (out of which, the first eight represent the scaling coefficients) in addition to the eight remaining scaling coefficients of the fine signal. Since no equivalent scales are available, the remaining 24 (9–32) of the 32 coarse coefficients are retained; in contrast, the first eight coefficients of the compound matrix are chosen to equal scaled values of the corresponding eight scaling coefficients of the fine signal, with the scaling factor similar to the definition of Es in the previous paragraph.

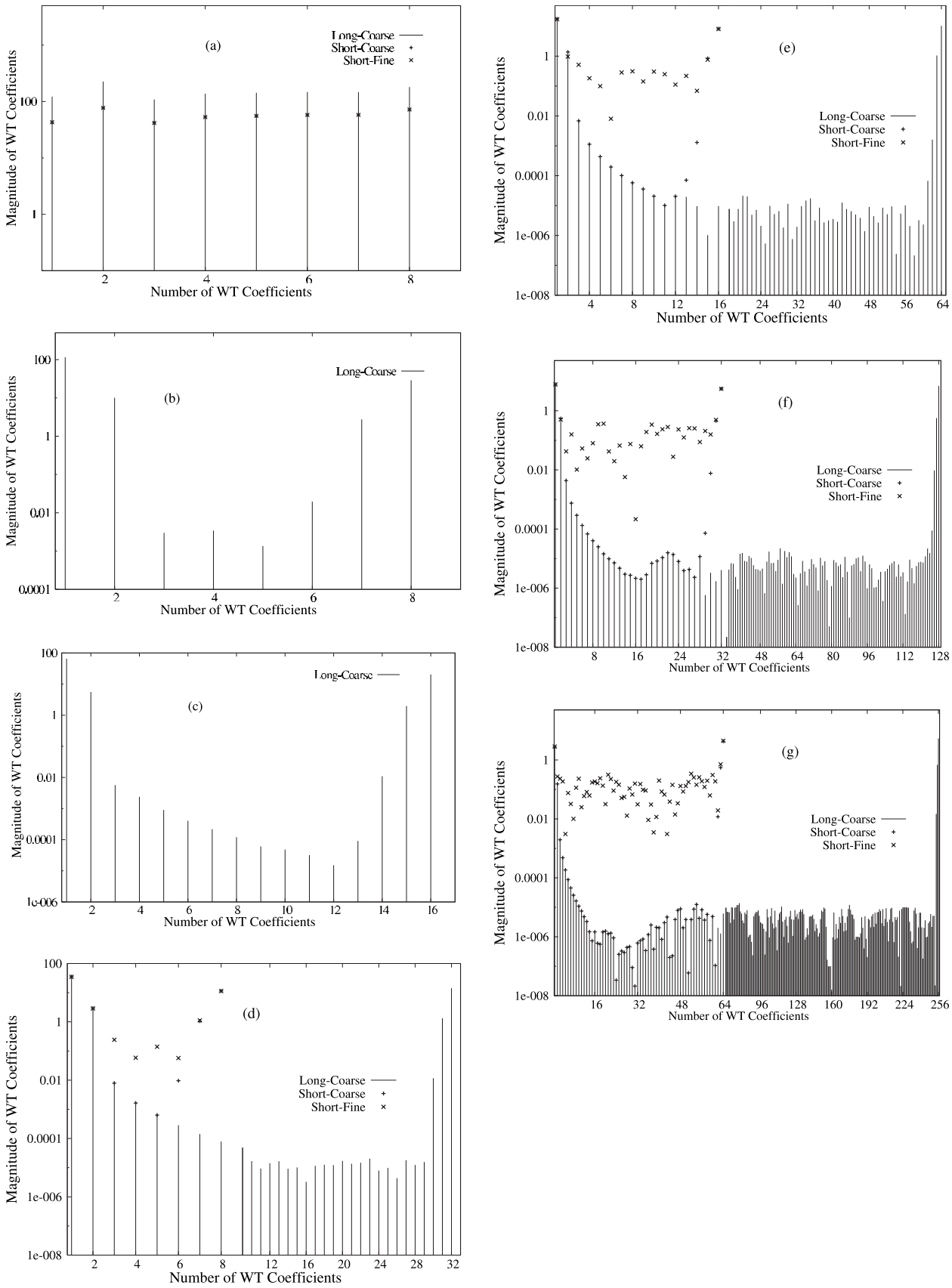

FIG. 4. Magnitude of WT coefficients at different stages (excluding the first stage) of decomposition of a 1024 data-set logarithmic signal as given in Fig. 3. Except for the initial and final three coefficients, note that the short-coarse coefficients coincide with the long-coarse coefficients and are always found right on top of the impulses that represent the long-coarse coefficients.

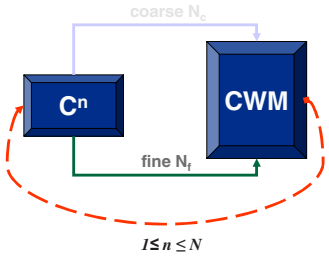

FIG. 5. (Color online) Illustration of the dCWM algorithm.

This method of repetition, scaling and replacement of the coefficients, enforces transferability of almost all fine information (excepting the repeated boundary coefficients), while ensuring an "informed" modification of the end boundary coefficients and the scaling coefficients, which combine in tandem to enable the suitable extension of trends exhibited by the short-time fine trajectory.

(6) *Compounding*. The selected WT coefficients are assembled to form a compounded matrix (vector in this case) that has both coarse and fine WT coefficients, ready for inversion.

(7) *Reconstruction.* The hybrid signal is now obtained via a series of convolution operations involving the compound matrix (vector) and the synthesis matrix.

The relative number of overlapping scales affects the quality of the compounding; larger number of overlap scales leads to a better description of the fine-signal features, while a decrease in the number of overlap scales with respect to the total number of scales leads to reduction in the accuracy of the description of fine-signal features.

An important as well as a distinguishing feature between the previous implementations of CWM and the concepts discussed here is the rescaling of the eight mother-wavelet coefficients by the respective *Es*. This ensures that the resultant compounded trajectory represents a logical projection of the shorter-fine trajectory extended in time consistent with the short-time behavior of the fine and coarse systems (while still retaining all fine-scale features), in contrast to the straightforward imposition of the fine-trajectory fluctuations onto the coarse-trajectory as was proposed in the earlier CWM methods.

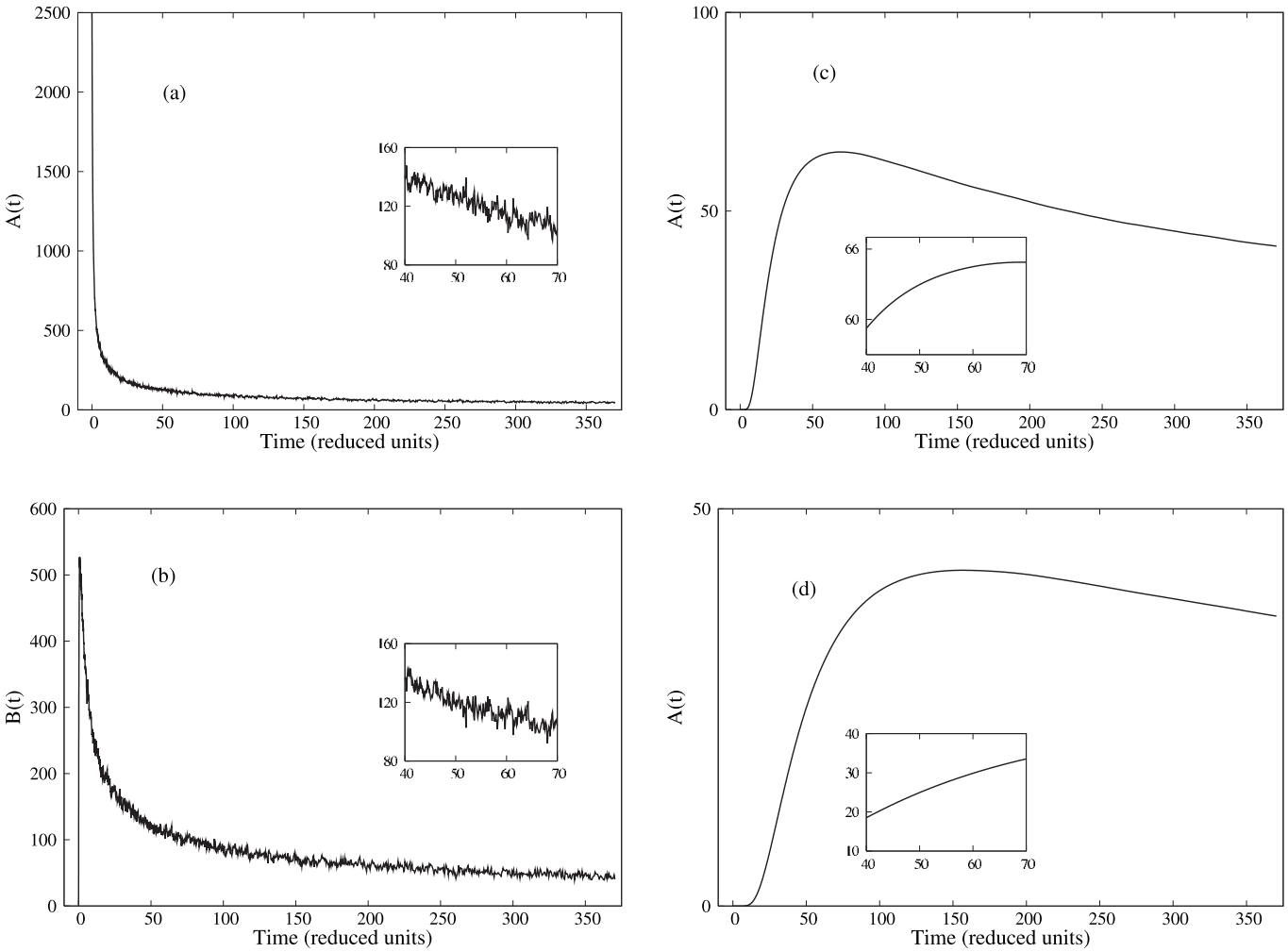

FIG. 6. (a) and (b) represent the fine-method variation in concentration of species A and B, respectively, with time. Note the fluctuations in the fine signal. (c) and (d) represent the time variation in concentration of species *A* at nodes=50 and 100, respectively. The insets illustrate the variation in concentration within a much narrower period of time. Note: *y*-axis scale is not constant across the plots.

C. Dynamic-CWM (dCWM) approach

The dCWM method extends the CWM approach to enable the concurrent coupling of different scale-specific methods by dynamically combining the fine and coarse simulation methods over successive subintervals (dynamic updates) to obtain the compound trajectory. At each dynamic step, the fine and the coarse trajectories are coupled via CWM, and the resulting end point of the compound signal in trajectory space becomes the starting point (initial condition) for computing the next set of trajectories respectively; this procedure is then repeated for the desired number of intervals as illustrated in Fig. 5. dCWM has the advantage of inherently coupling the dynamics of each method, in addition to lending further stochasticity to the compound trajectory, which could lead to a better exploration of the trajectory-space. Furthermore, in the earlier formulations, it was implicitly assumed that the fluctuations obtained from the fine signal, which was evaluated over much shorter time, was representative of fluctuations occurring over a much longer duration. This is not necessarily true as the magnitude as well as the nature of fluctuations can and in general does change as the system evolves. This is overcome in the dCWM approach, since the fine method is employed at various stages of the evolution of the system. At the same time, the advantages of the CWM method are retained, without any measurable increase in computational expense.

D. Model reaction-diffusion system

As a model system, two species A and B that participate in a first-order reversible reaction occurring at a surface as given in Eq. (2) are considered:

$$A \underset{k_{ba}}{\overset{k_{ab}}{\leftrightarrow}} B. \tag{2}$$

The surface represents the boundary of a semi-infinite positive half space, with the half-space suitably discretized to handle diffusion of both species to and from the reactive surface. For convenience, the two reaction rates k_{ab} and k_{ba} are set to equal unity, and the initial concentration of A at the reactive surface is chosen to be much larger in order to bias the forward reaction to be more active at the initial stages of the diffusion-reaction process. Further, initial concentration of both species is set to zero everywhere other than at the reactive surface. Our numerical model of the system is 1D in space, such that the diffusion domain is discretized into line increments and nodes, and the reactive surface is represented by a single boundary node. The infinite extent of the diffusion domain is approximated by choosing a sufficiently large length and large number of nodes such that for the duration of the simulations, there is no change in concentration of species at nodes far from the reactive boundary and that concentration remains equal to zero.

Two levels of description (coarse and fine) are used. The accurate "fine" method employs the stochastic kinetic Monte Carlo (KMC) method [21] in conjunction with finite differences to simulate the chemical reaction at the reactive boundary and diffusion, respectively, while using relatively smaller time increments as dictated by KMC. In contrast, the coarse method models both reaction and diffusion deterministically using much larger time increments, thereby addressing much larger temporal dimensions, in a less precise fashion. In contrast, for simplicity, both coarse and fine spatial dimensions as well as spatial discretizations are taken to be the same.

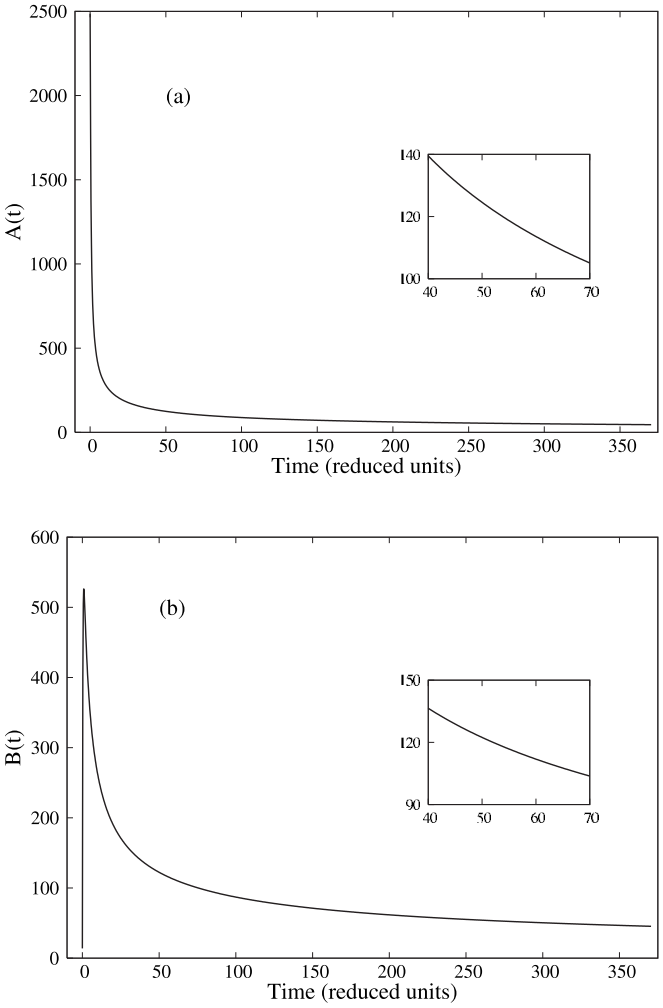

FIG. 7. (a) and (b) represent the coarse-method variation in concentration of species A and B, respectively, with time. The insets illustrate the variation in concentration within a much narrower period of time.

Using an explicit Euler scheme, the diffusion equation [Eq. (3)] for species diffusion is solved numerically, where C_s and D_s represent the species concentration ($[A]$ and $[B]$) and their respective diffusion constants. The size of the time step for the fine method is obtained from KMC calculations (described below), while the coarse time step is chosen to be a multiple of the fine time-step size. The flux of the diffusing species is set to zero at the boundary node (i.e., at the reactive site)

$$\frac{\partial C_S}{\partial t} - D_S \nabla^2 C_S = 0. \tag{3}$$

In the fine model, the occurrence of the two reactions [Eq. (2)] at the reaction site is determined stochastically via KMC

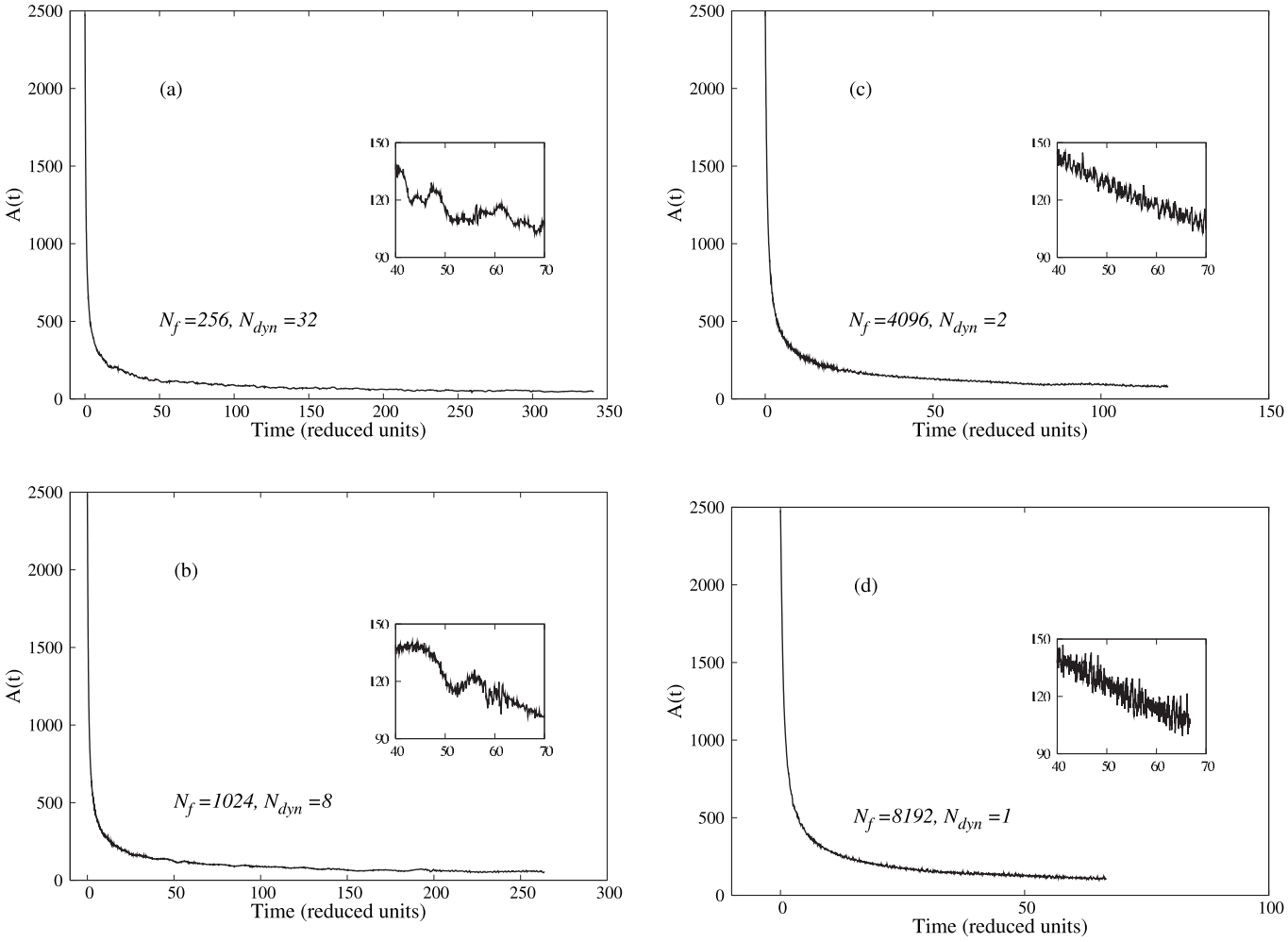

FIG. 8. Time-variation in concentration of species A for $Mp=8$ and different values of N_f and N_{dyn} such that their product is constant. The insets illustrate the variation in concentration within a much narrower period of time.

based on Gillespie's stochastic simulation algorithm [21]. The reaction times for both reactions are given by

$$\delta t_{ab} = -\log(1-R_1)/[A]k_{ab}, \tag{4}$$

$$\delta t_{ba} = -\log(1-R_2)/[B]k_{ba}, \tag{5}$$

where R_1, and R_2 are distinct numbers obtained from a uniform random number distribution and $[A]$ and $[B]$ represent the atomic and molecular concentrations of the respective species. The occurrence of either one of the reactions is decided by the minimum of the two reaction times as given by the following equations. If

$$\delta t_{ab} < \delta t_{ba}, \quad \begin{matrix}[A]=[A]-1,\\ [B]=[B]+1,\end{matrix} \tag{6}$$

while if

$$\delta t_{ba} < \delta t_{ab}, \quad \begin{matrix}[A]=[A]+1,\\ [B]=[B]-1.\end{matrix} \tag{7}$$

Next, the smaller of the two times is chosen to be the size of the time step for solving the diffusion equation. If the resultant time step size (Δt) is found to be incompatible with the Courant condition for numerical stability of the diffusion equation, i.e., if $\Delta t > \Delta x^2/2D_S$, where Δx is the size of the finite difference element, Δt is then subdivided into smaller time steps as follows:

$$\Delta t = n_t \Delta t' + dt',$$

$$n_t = \mathrm{int}(\Delta t/\Delta t'), \tag{8}$$

where $\Delta t' = \Delta x^2/2D_S$.

At every dynamic step, the fine simulation is propagated for N_f time steps and a resultant variation in concentration of the two species at all nodes is obtained as a function of time. Keeping in mind that KMC results in unequal spacings in time, a spline interpolation routine is invoked to get the concentration variation as a function of equally spaced time steps (Δt_f). Once Δt_f is obtained, Δt_c is evaluated ($=R\Delta t_f$) and the coarse signal is propagated for N_c time steps.

In the coarse simulation, the concentration of each species at the reaction site is obtained deterministically in a straightforward fashion from the respective reaction rates [Eq. (9)] using a finite difference scheme. Once the coarse and fine responses are obtained, the steps enumerated in the section

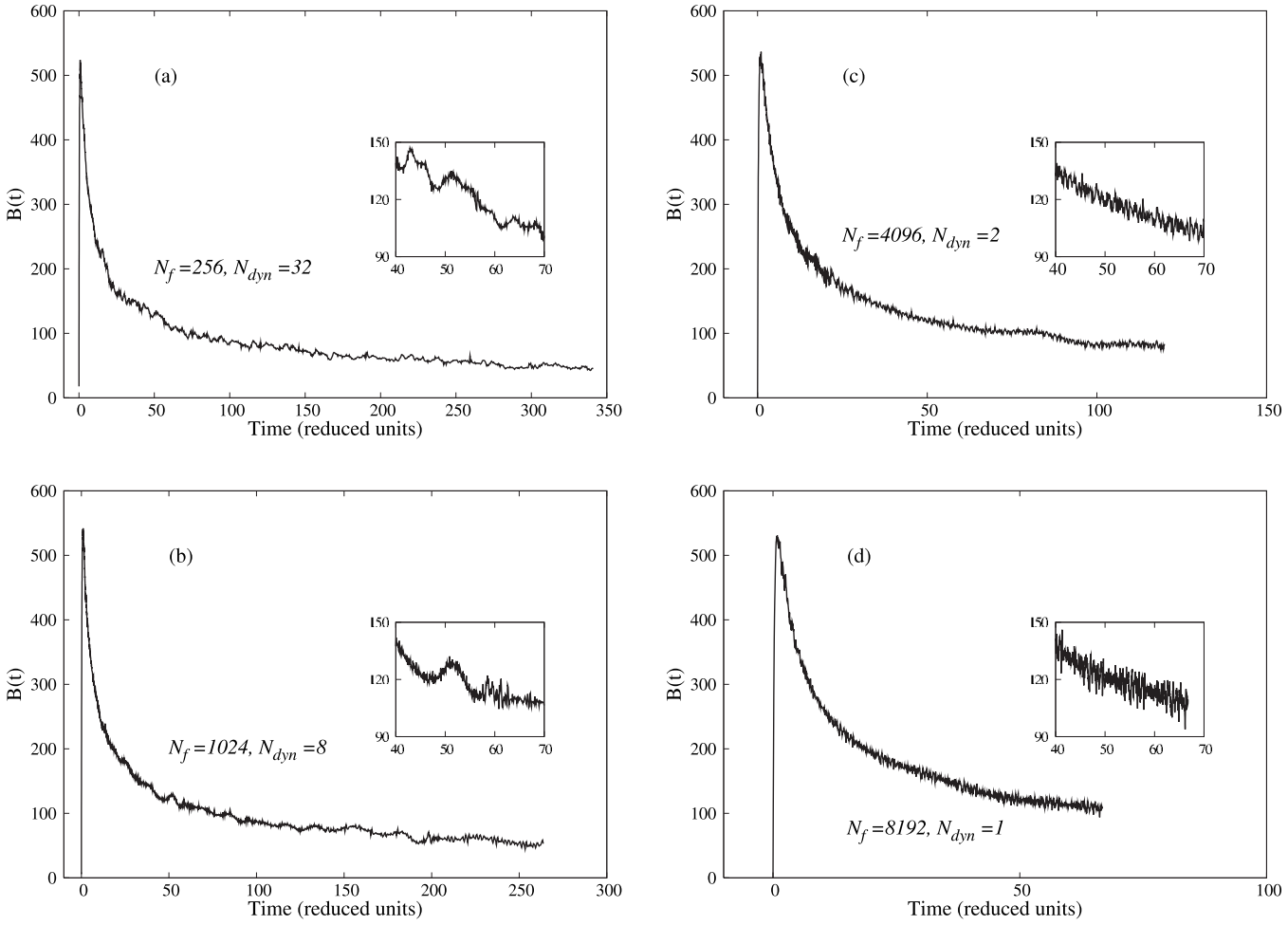

FIG. 9. Time variation in concentration of species B for $Mp=8$ and different values of N_f and N_{dyn} such that their product is constant. The insets illustrate the variation in concentration within a much narrower period of time.

on CWM is used to form the compounded matrix (vector), with which the compound trajectory for the given dynamic step is obtained, with the final concentrations of each species at all nodes being the starting concentrations for the next set of coarse and fine calculations:

$$A(t+\Delta t) = A(t) - k_{ab}A(t)\Delta t + k_{ba}B(t)\Delta t,$$

$$B(t+\Delta t) = B(t) + k_{ab}A(t)\Delta t - k_{ba}B(t)\Delta t. \qquad (9)$$

III. RESULTS AND DISCUSSIONS

A principal objective of this work is to examine and present the advantages of using the dCWM framework for multiscale simulations such as the 1D reaction-diffusion problem described above. The model system under study is made simple enough, so that a stochastic "fine" simulation of the reaction-diffusion process (i.e., until the system attains chemical equilibrium), is possible. Thus one can benchmark and quantify the ability of the dCWM framework to emulate the multiscale behavior of the system.

As a first step, the problem is modeled using the (i) stochastic fine method and the (ii) deterministic coarse method. In each case, the number of nodes (i.e., extent of spatial discretization) equaled 1000 and the size of each node was 0.0625 in arbitrary units of length (l); note that, in addition, time was also expressed in arbitrary units (t). Thus the units of concentration are expressed as *atoms/l*, while the units of the diffusion constant are expressed as l^2/t. The initial concentration of $[A]$ and $[B]$ at the reactive site was set to 2500 and zero, respectively, while the respective concentrations at all other sites were identically set to zero. The diffusion constant of both species was chosen to be the same and equaled 0.01. Figure 6(a) and 6(b) present the long-time variation in concentration of $[A]$ and $[B]$ at the reactive site as obtained from the fine method (KMC+ finite differences); the simulation was carried out until there was a net saturation in the respective concentrations, though there was still the persistent presence of fluctuations in both trajectories. To achieve equilibrium 65 536 time steps were used, with the spline-interpolated time-step size equaling $5.66\times10^{-3}t$ (total time= 371.0 t). The overall trend (i.e., the mean trajectory) was independent of the choice of the random-number seed, while there were very minor differences in the occurrence of fluctuations for different random-number seeds. Also, the amount of fluctuations greatly diminished with distance from the reaction site [Figs. 6(c) and 6(d)] and in addition, far

TABLE I. Values of various simulation parameters used for the case when $M_p=8$ and $N_f \times N_{\mathrm{dyn}}$ are constant.

$M_p=8$	N_{dyn}	N_f	N_c	Total time (t)
$N_f \times N_{\mathrm{dyn}}=$**8192**	32	256	2048	341.3
$N_c \times N_{\mathrm{dyn}}=$**65536**	8	1024	8192	264.0
	2	4096	32768	120.2
	1	8192	65536	66.8

away from the reactive site, the concentrations essentially remained zero. As a study in contrast, a full deterministic simulation was carried out for the same number of time steps and the same time-step size as that of the fine method. Clearly, as evident from Figs. 7(a) and 7(b), the fluctuations characteristic of the fine method were absent from the respective coarse trajectories.

Having the results at both ends of the scale spectrum, i.e., the results as obtained using the accurate stochastic fine method and the purely deterministic coarse method, attention is turned to examining the ability of the dCWM approach to model the reaction-diffusion process accurately. The dCWM method depends critically on the choice of N_f and the number of dynamic updates (N_{dyn}). Ideally, as the system evolves in time, the fine simulation has to be invoked as frequently as possible to enable sampling at various points in phase space, while N_f has to be large enough to capture the stationary fine-scale fluctuations as and when the fine simulation is invoked. Since $N_f \times N_{\mathrm{dyn}}$ represents the total number of fine computations, it would be judicious to maximize N_{dyn} and reduce N_f as much as possible to limit any redundancy in the fine computations, while still being able to capture all essential physics inherent to the fine simulation at different stages of the simulation for a given number of fine computations. Equally important choices are that of M_p ($=I_c/N_f$) in tandem with N_c, as implicitly, it is assumed that the fluctuations captured over N_f time steps are stationary over the time equaling $M_p \times N_c$. In order to comprehensively characterize the importance of the different simulation parameters as well as also to aid comparison between the dCWM and the above-discussed stochastic and deterministic results, the following were investigated: (i) The interplay between N_f and N_{dyn} for a given number of total fine ($N_f \times N_{\mathrm{dyn}}$) and coarse ($N_c \times N_{\mathrm{dyn}}$) computation steps and (ii) the importance of the relative number of scales beyond overlap (or equivalently M_p) for a given N_f. Note that for all investigations, the compound trajectory obtained via the dCWM method consisted of 65536 points—same as the pure coarse and fine trajectories.

As a first part to this study, the interplay between N_f and N_{dyn} for a fixed value of M_p and a given number of fine computation steps ($N_f \times N_{\mathrm{dyn}}$) is investigated. Obviously, N_c equals $M_p \times N_f$. Figures 8 and 9 illustrate the variation of the two concentrations at the reactive site for the specific value of $M_p=8$ and different combinations of N_f and N_{dyn}, while Table I gives the list of values of N_f, N_{dyn}, and N_c used in Figs. 8 and 9. It has to be pointed out that the time-step size for the coarse method was set to equal that of the spline-interpolated fine method time-step size at each dynamic step, thereby avoiding the need for interpolation of the coarse information at each dynamic step.

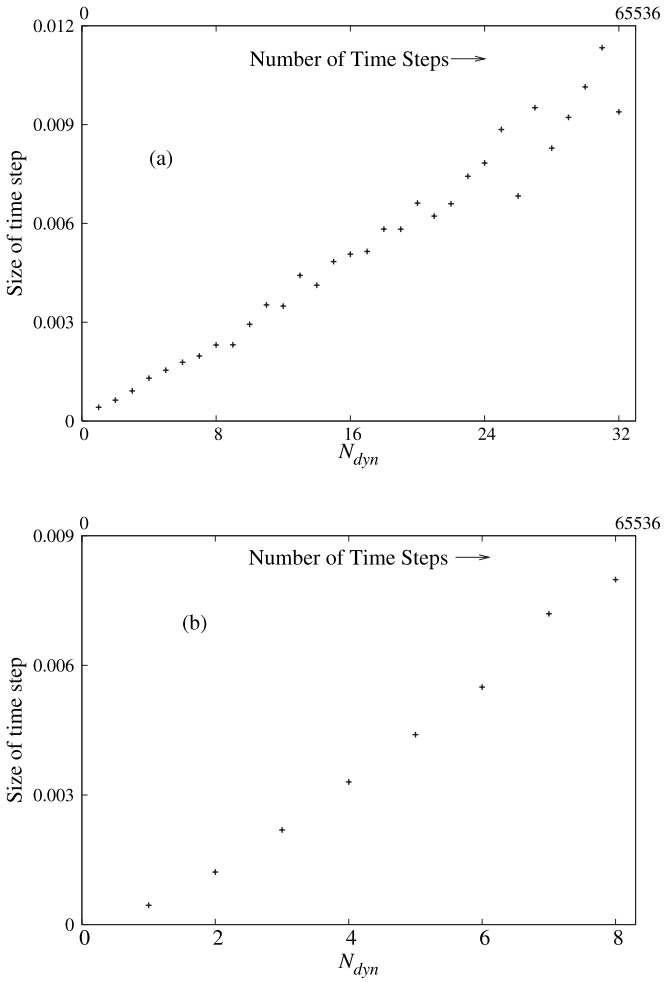

FIG. 10. Variation in size of time step as a function of the number of dynamical steps for (a) $N_{\mathrm{dyn}}=32$ and (b) $N_{\mathrm{dyn}}=8$.

A central observation regarding the effect of N_{dyn} and N_c emerges; for a given number of coarse-computation steps (i.e., 65 536 points) and fine-computation steps ($=N_{\mathrm{dyn}} \times N_f$), the amount of time addressed in each case increases with increasing N_{dyn} (or decreasing N_f) as noted in Table I. The fact that during the initial stages of each case, there is a monotonic and a relatively rapid decrease (or increase) in the concentration of A (or B) at the reactive site, indicates that, initially, the forward reaction is selectively preferred by KMC. More importantly, at the initial stages, relatively much smaller time-step sizes are selected by KMC due to the higher concentration of $[A]$ [see Eqs. (4) and (5)], while in the later stages, the probability of occurrence of larger time steps is much higher. This fact is reflected in Fig. 10, which depicts the variation in the time-step size (evaluated at the end of every N_f fine computations), as a function of the number of dynamic steps. Thus, for cases involving large N_f (and therefore large N_c, for a given M_p), where the dynamic updates occur ***less*** frequently, smaller time-step sizes are used over much larger chunks of computational steps, leading to much smaller time coverage. In fact, for the $N_{\mathrm{dyn}}=1$ case, which represents the original CWM approach, the least time-coverage can be seen. Also, the dependence of total-time coverage was very weakly dependent on

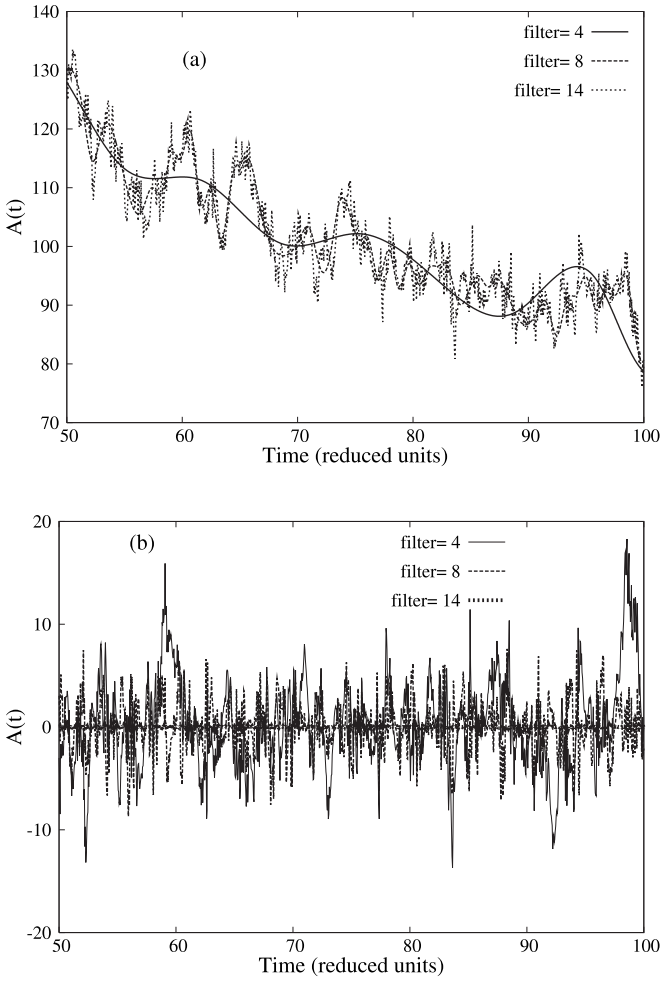

FIG. 11. (a) Time variation in the (a) coarse and (b) fine components of species A concentration for different values of the scale filter for the $N_{\mathrm{dyn}}=2$ dCWM trajectory.

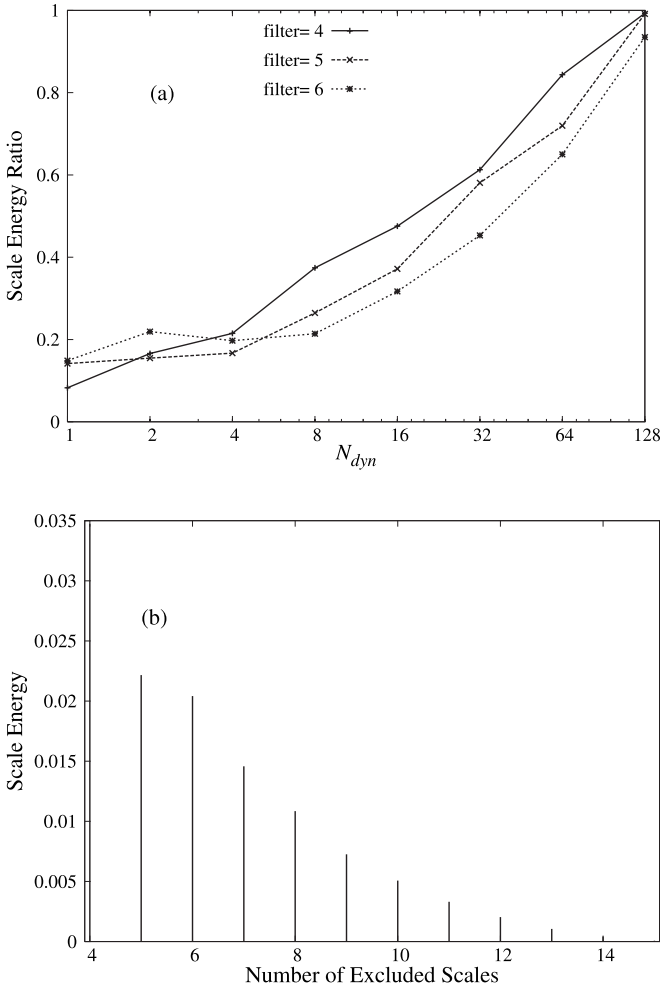

FIG. 12. (a) Variation in the relative energy of different dCWM trajectories as a function of N_{dyn} for three different values of the scale filter. (b) Scale-energy variation of the benchmark signal; here the number of excluded scales represents the value of the scale filter.

the choice of the random-number seed (for KMC), and any difference in the times were negligible for all practical purposes.

The importance of N_{dyn} is shown by the insets of Figs. 8 and 9. One can observe clear differences in the overall shape of the concentration variation as a function of N_{dyn}. Particularly, for larger N_{dyn}, there are distinct oscillatory features (as pointed out in the inset figures), similar in nature to those present in the fine trajectories (Fig. 6), that are noticeably absent in the other cases; in other words, if one were to compare the CWM [Figs. 8(d) and 9(d)] and the dCWM results, it is obvious that, in addition to larger time coverage, trends characteristic of the concentration variations which were not captured by the CWM approach are described by the dCWM method.

Next, the role of nonoverlapping scales (S_B) and M_p (for a given N_f) in controlling the accuracy of the resulting trajectories is examined. Table II lists the values of M_p, S_B, N_{dyn}, and N_c used in investigations for a specific value of N_f(=256) as well as the number of overlapping scales (S_O). As expected, there was a noticeable dependence of the total time coverage on N_{dyn} (and M_p) as given in Table II. For smaller values of N_{dyn} the dependence was much stronger and, for large values of N_{dyn} ($\geq$32), the total time-coverage approached that of the full-fine simulation.

The variations in dCWM with respect to the amount of very fine-scale fluctuations and coarser-scale oscillatory trends were examined for different N_c (therefore different

TABLE II. Values of various simulation parameters used for the case of N_f=256.

Total time steps=65536	N_{dyn}	M_p	N_c	S_B	Total time (t)
	128	2	512	1	365.2
	64	4	1024	2	350.0
$\boldsymbol{N_f}$=256	32	8	2048	3	341.3
$\boldsymbol{S_o}$=**5(8−3)**	16	16	4096	4	308.0
	8	32	8192	5	250.4
	4	64	16384	6	180.9
	2	128	32768	7	83.6
	1	256	65536	8	27.5

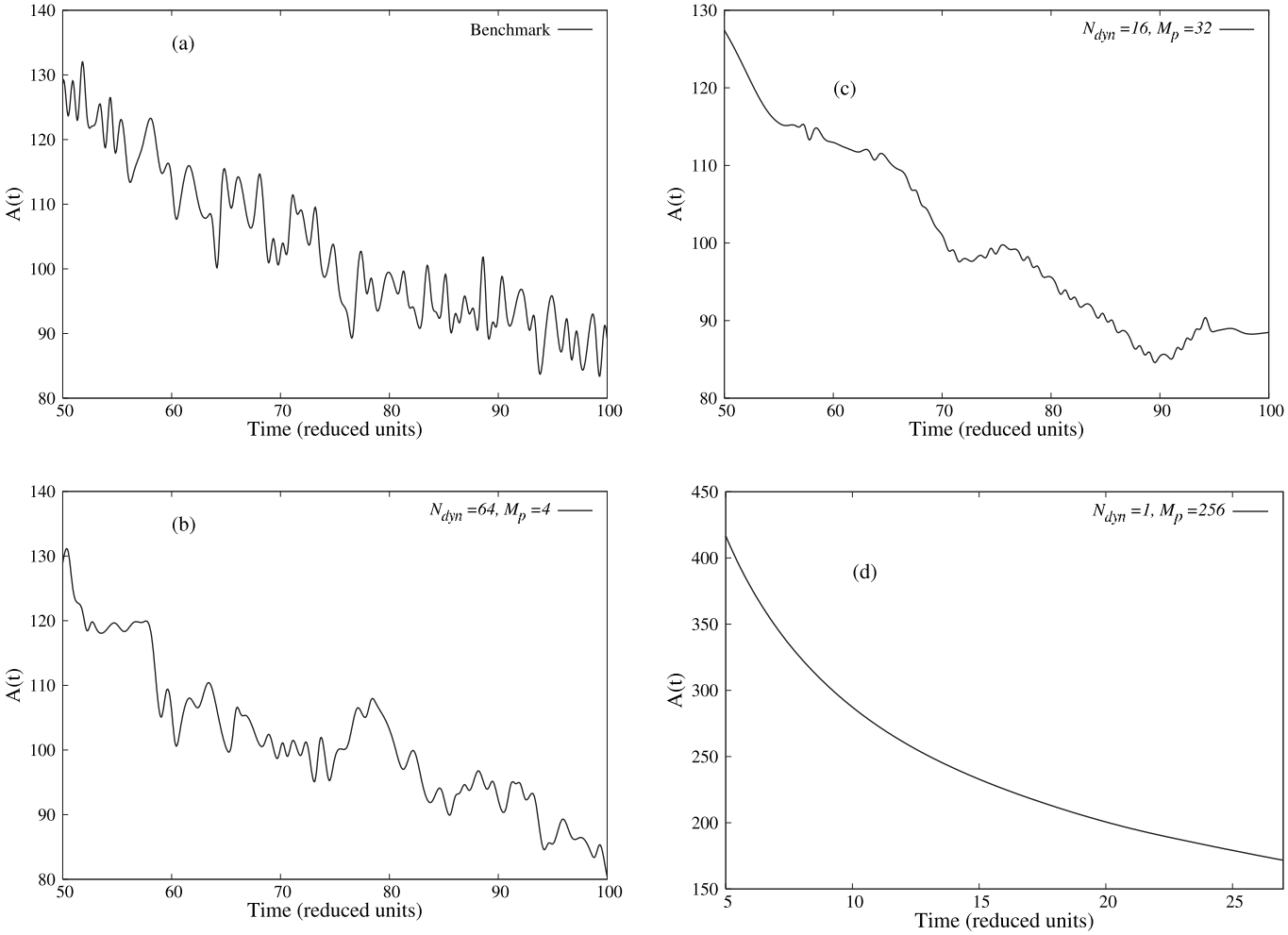

FIG. 13. Time variation in the coarse components of concentration of species A for different values of N_{dyn} and M_p for a fixed value of N_f=256 as obtained for scale filter equal to 10.

S_B), N_{dyn}, and M_p. Recognizing the effectiveness of wavelets as scale-filters, the contributions of different scales to the composition of each trajectory can be examined via the padding technique discussed previously. For instance, the mean trend of each trajectory can be filtered out by removing the coarsest-scale contributions, enabling the quantification of the fluctuations corresponding to the finer scales, or in contrast, the fine-scale fluctuations could be filtered out, while retaining the larger-scale oscillatory contributions to the overall trajectory. The following steps were used to examine the effect of the various scales.

(1) Interpolating all trajectories using splines to ensure equivalent time-step sizes. This is done since each trajectory corresponds to different time-coverages and consequently different time-step sizes. All resulting trajectories are now resampled at the time-step size as that of the "N_{dyn}=1" case, and leads to a one-to-one comparison between each dCWM trajectory and the benchmark, for the time coverage of the given dCWM trajectory.

(2) Next, the padding technique is invoked to scale separate the finer and coarser information available for each trajectory. For extracting "coarse" information, all coefficients beyond a cutoff scale are set to zero, while the opposite is done to obtain "fine" information. This allows the ability to clearly demarcate the different scale contributions.

As an example of the above method, consider Figs. 11(a) and 11(b), which present the "N_{dyn}=128" trajectory of species [A] when reconstructed selectively by inclusion of specific scales. Clearly, the resultant coarse trajectory [Fig. 11(a)] obtained by excluding all scales greater than 4 (2^4 =16) is (almost) devoid of any fluctuations, while the frequency and magnitude of fluctuations increase with inclusion of additional finer scales. The exact opposite behavior is seen for the corresponding fine-components [Fig. 11(b)], with maximum stationary fluctuations present when scale filter (i.e., number of excluded scales) equals 4. Thus, in order to characterize the quality of each dCWM trajectory, the respective fine components obtained at very small values of the scale filter (4–6), were examined and the "energy" corresponding to the transferred fine fluctuations was evaluated by calculating the average intensity of the fluctuations for each case. The average intensity was in turn, evaluated by calculating the square root of the sum of squares of the magnitudes of fluctuations over the time domain of each trajectory and then averaging it over the total number of time steps.

Depending on the time coverage of the different dCWM trajectories, the corresponding average intensity of the benchmark trajectory was evaluated, thereby enabling the quantification of energy transfer expressed as a ratio of the corresponding dCWM intensity to the benchmark intensity [see Fig. 12(a)]. In Fig. 12(a), for trajectories with $N_{\mathrm{dyn}} \geq 8$, the energy was evaluated over 524 288 (2^{19}) points resampled at the $N_{\mathrm{dyn}}=1$ time-step size, while 262 144, 131 072, and 65 536 points were used for $N_{\mathrm{dyn}}=4$, 2, and 1, respectively. Also, note that for a given choice of N_{dyn} (and other related parameters), and a given value of the scale filter, the calculated energies were very similar for different values of the random-number seed (five different trajectories for each case were considered), and the standard deviation in the scale energy was less than 1.0%. Figure 12(b) provides information on the energy contained in each scale for the benchmark trajectory evaluated over 524 288 points; this can be used for the purposes of estimation of scale energy for the different dCWM trajectories when used in conjunction with Fig. 12(a).

As expected, Fig. 12(a) shows a strong correlation between the energy ratio and N_{dyn}, such that with increasing N_{dyn}, there is a parallel increase in the energy of the corresponding trajectories; in fact the energy of the $N_{\mathrm{dyn}}=128$ trajectory is remarkably similar to the benchmark for the three different scale filters given. Since the computational cost for the fine method is the most expensive, one can relate M_p (and N_{dyn}) in tandem with the ability of the corresponding trajectories to emulate the benchmark, to be a measure of the computational efficiency of the dCWM method. Obviously, the benchmark stochastic simulation is the most computationally expensive calculation, while at the other end is the nondynamic CWM simulation where $N_{\mathrm{dyn}}=1$ ($M_p=256$).

Figure 12(a) in conjunction with Table II, show that 65% of the benchmark energy is replicated with a time coverage of 90% of the benchmark time for one-eighth of the computational cost ($M_p=8, N_{\mathrm{dyn}}=32$). With a computational savings of a factor of 4, i.e., $M_p=4$, $N_{\mathrm{dyn}}=64$, 85% of the benchmark energy is captured with a corresponding 92% time coverage, while for $N_{\mathrm{dyn}}=2$ or equivalently for half the computational cost of the benchmark, there is almost 100% efficiency. These results accentuate the fact that the quality of the trajectories depends intimately on the choice of N_{dyn}, S_B, and M_p; an increase in fine computations ($N_{\mathrm{dyn}} \times N_f$) leads to a marked improvement in the quality of the trajectory as evidenced in Fig. 12(a) as well as in Fig. 13, which depicts select dCWM "coarsened" trajectories devoid of the very-fine "white-noise" components, and evaluated at scale filter $=10$.

For large S_B (i.e., scales beyond overlap), the deterministic coarse behavior dominates, thereby suppressing the coarser-scale contributions of the fine method toward shaping the trends of the dCWM trajectory. An equally important reason for the dominance and suppression of either method is the fact that there are $(M_p-1)\times 6$ replacements of the fine-method coefficients by the scaled coarse-method coefficients at each scale, and at larger M_p, this effect is more pronounced leading to considerable loss in transfer of the fine-method information.

IV. CONCLUSIONS

This paper introduces and discusses the workings of the wavelet based dCWM method, for coupling two or more scale(s)-specific methods in a dynamic and seamless fashion to realistically model any system that requires a temporal multiscale representation. A simple, yet representative 1D reaction diffusion process is examined in order to illustrate the multiscale capabilities of the dCWM method. The results clearly indicate that the dCWM method is capable of reproducing many aspects of the true behavior of the simulated system for a lower computational cost. The dCWM method can be readily extended in a nontrivial yet a straightforward way to model far more complex multiscale phenomena in a computationally efficient fashion by combining different levels of spatiotemporal description of the constituent degrees of freedom. In addition, combining dCWM with other multiscale methods such as PIT [10] could lead to substantial reduction in computational overhead. PIT is a technique where the system is initially modeled by the coarse method; next, the coarse trajectory of the system is broken up into a series of smaller segments, with the initial conditions of each segment serving as starting points for the fine method. Computing the more accurate trajectories (by the fine method) from these starting points are then done in parallel, till the respective end points are reached. dCWM can be used as a "speed-up" tool by employing it on each segment, thereby getting accurate trajectories further reducing computational cost.

ACKNOWLEDGMENTS

This research was sponsored by the Mathematical, Information, and Computational Sciences Division, Office of Advanced Scientific Computing Research, U.S. Department of Energy with Anil Deane as the program manager. The work was partly performed at the Oak Ridge National Laboratory, which is managed by UT-Battelle, LLC under Contract No. De-AC05-00OR22725. Discussions with M. Syamlal, T. J. O'Brien, and D. Alfonso of the National Energy Technology Laboratory (NETL), Stuart Daw of Oak Ridge National Laboratory, and Rodney Fox and Z. Gao of Iowa State University have been very useful.

[1] X. E. B. Enquist, Commun. Math. Sci. **1**, 87 (2002).
[2] V. Shenoy, R. Miller, E. B. Tadmor, D. Rodney, R. Phillips, and M. Ortiz, J. Mech. Phys. Solids **47**, 611 (1999).
[3] I. G. Kevrekidis, Commun. Math. Sci. **14**, 715 (2003).
[4] R. E. Rudd and J. Q. Broughton, Phys. Rev. B **58**, R5893 (1998).
[5] F. Abraham, J. Broughton, N. Bernstein, and E. Kaxiras, Europhys. Lett. **44**, 783 (1998).
[6] G. Frantziskonis and P. A. Deymier, Modell. Simul. Mater. Sci. Eng. **8**, 649 (2000).
[7] G. Frantziskonis, Probab. Eng. Mech. **17**, 359 (2002).
[8] G. Frantziskonis and P. Deymier, Phys. Rev. B **68**, 024105 (2003).
[9] G. Frantziskonis, S. K. Mishra, S. Pannala, S. Simunovic, C. S. Daw, P. Nukala, R. O. Fox, and P. A. Deymier, Int. J. Multiscale Comp. Eng. **4**, 755 (2006).
[10] L. Baffico, S. Bernard, Y. Maday, G. Turinici, and G. Zerah, Phys. Rev. E **66**, 057701 (2002).
[11] A. Arneodo, G. Grasseau, and M. Holschneider, Phys. Rev. Lett. **61**, 2281 (1988).
[12] L. Telesca, V. Lapenna, and N. Alexis, Chaos, Solitons Fractals **22**, 741 (2004).
[13] S. N. Zhao, X. Y. Xiong, X. H. Cai, and F. Hu, Europhys. Lett. **69**, 81 (2005).
[14] D. F Martin, P. Colella, M. Anghel, and F. J. Alexander, Comput. Sci. Eng. **7**, 24 (2005).
[15] T. Yanai, G. I. Fann, Z. Gan, R. J. Harrison, and G. Beylkin, J. Chem. Phys. **121**, 2866 (2004).
[16] C. K. Chui, *An Introduction to Wavelets*, (Academic Press, London, 1992).
[17] I. Daubechies, Commun. Pure Appl. Math. **41**, 909 (1988).
[18] I. Daubechies, *Ten Lectures on Wavelets* (CIAM, Philadelphia, PA, 1992).
[19] S. G. Mallat, IEEE Trans. Pattern Anal. Mach. Intell. **11**, 674 (1989).
[20] A. Harbo-Cour and A. Jensen, *Ripples in Mathematics: The Discrete Wavelet transform* (Springer, New York, 2000).
[21] D. T. Gillespie, J. Phys. Chem. **81**, 2340 (1977).